



TITLE:

Direct observation of local chemical ordering in a few nanometer range in CoCrNi medium-entropy alloy by atom probe tomography and its impact on mechanical properties

AUTHOR(S):

Inoue, Koji; Yoshida, Shuhei; Tsuji, Nobuhiro

CITATION:

Inoue, Koji ...[et al]. Direct observation of local chemical ordering in a few nanometer range in CoCrNi medium-entropy alloy by atom probe tomography and its impact on mechanical properties. *Physical Review Materials* 2021, 5(8): 085007.

ISSUE DATE:

2021-08



URL:

<http://hdl.handle.net/2433/282055>

RIGHT:

©2021 American Physical Society

Direct observation of local chemical ordering in a few nanometer range in CoCrNi medium-entropy alloy by atom probe tomography and its impact on mechanical properties

 Koji Inoue,¹ Shuhei Yoshida ² and Nobuhiro Tsuji ²
¹*Institute for Materials Research, Tohoku University, Oarai, Ibaraki 311-1313, Japan*
²*Department of Materials Science and Engineering, Kyoto University, Yoshida-Honmachi, Sakyo-ku, Kyoto 606-8501, Japan*


(Received 28 April 2021; revised 23 July 2021; accepted 11 August 2021; published 26 August 2021)

Local chemical ordering in CoCrNi medium-entropy alloy (MEA) was directly observed by the use of atom probe tomography. It was found that the densities of Cr, Co, and Ni were almost the same along the [111] direction, while those along the [001] direction were modulated to take a slightly enhanced and depleted value alternately within approximately 10 atomic layers corresponding to about 2 nm. The degree of modulation of Co and Ni was stronger than that of Cr. It was suggested that Cr-rich {001} atomic layers and (Ni + Co)-rich {001} layers tended to align mutually in the face-centered-cubic CoCrNi solid solution alloy. The mechanical properties of the MEA was found not to be affected by the presence of the local chemical ordering.

 DOI: [10.1103/PhysRevMaterials.5.085007](https://doi.org/10.1103/PhysRevMaterials.5.085007)

I. INTRODUCTION

The concept of alloy systems using multiple principal elements with a high degree of configurational entropy has received considerable attention over the past decade. Such multielemental alloys are usually termed as high-entropy alloys (HEAs). HEAs are defined, in a narrow sense, as single-phase solid-solution alloys with equiatomic composition consisting of more than five kinds of elements. Broad definition of HEAs includes concentrated alloys with chemical compositions in the middle of composition space of phase diagrams, even if they are deviated from the equiatomic compositions or contain secondary phases. All these HEAs have been energetically studied due to intriguing combination of properties such as high strength and high fracture toughness, and are considered as a new class of structural metallic materials [1–4]. The most famous HEA is the CrMnFeCoNi alloy, which is often called Cantor alloy [5]. The CrMnFeCoNi alloy is a single-phase solid-solution alloy where five kinds of elements randomly distribute. Among the CrMnFeCoNi family of equicompositional face-centered-cubic (FCC) alloys, the CoCrNi single-phase alloy, which belongs to medium-entropy alloys (MEAs) consisting of three or four elements, exhibits the highest yield strength [6,7].

One key issue under passionate discussion in recent years is the presence of short-range ordering (SRO) or local chemical ordering (LCO) in the CoCrNi and its contribution to the high strength [8–10]. In general, a pair-correlation length for SRO is expected to be the order of a few nearest neighbor atom spacings. Therefore, a preferential local ordering of the elements more than a few nearest neighbor atom spacings is simply referred to as LCO in this manuscript. Zhang *et al.* [10] recently employed furnace-cooling with very slow cooling rate after heat-treatment at 1000 °C and found the diffuse scattering along the $\langle 111 \rangle$ direction in its diffraction pattern by energy-filtered transmission electron microscopy (TEM).

They argued that there was an increase in the yield strength (~ 50 MPa) of the CoCrNi due to the formation of SRO during cooling. It should be noted that the diffuse streaks in diffraction data are sensitive to SRO and SRO of binary alloys was originally quantified in such diffraction experiments by John Cowley (following Warren's x-ray studies), which is known as Warren-Cowley order parameters [11,12]. In contrast, another recent work on the CoCrNi alloy by Yin *et al.* [9] showed negligible difference between experimental yield strength in literature and theoretical value calculated under an assumption of perfect random solid solution. They concluded that the effect of SRO on the strength was negligible in the MEA processed under ordinary conditions (i.e., annealing above 600 °C followed by relatively fast-cooling (water-quenching or air-cooling)). However, it was uncertain whether SRO was present in the CoCrNi specimen used in their study. Thus, the effect of SRO on the high strength of the CoCrNi MEA reported to date is still unclear.

SRO in the CoCrNi MEA has been also reported by extended x-ray absorption fine structure (EXAFS) experiments [13]. The EXAFS analysis deduced that Cr in the solid-solution alloys had a tendency to bond with Ni and Co and to form SRO, but the interpretation relied on the DFT analysis, which was reported to be unreliable for the alloy system by other researchers [9]. Although the previous studies explained above gave us some hints about SRO in CoCrNi MEA, it is still under debate (1) whether SRO certainly exists or not, if it exists, (2) what kinds of structure it has, and (3) whether it affects mechanical properties or not. Therefore, the existence of SRO in the CoCrNi alloy and its impact on mechanical properties have not been perfectly confirmed yet.

In this work, we investigated the presence of SRO in the CoCrNi alloy using atom probe tomography (APT). APT can reconstruct a three-dimensional elemental map in a needle specimen with subnanometer spatial resolution and has a high mass-resolving capability that can distinguish even oxides,

TABLE I. Grain size, yield strength, ultimate tensile strength, uniform elongation, and total elongation of homogenized and annealed samples obtained by tensile tests at room temperature.

Material	Grain size	Yield strength	Tensile strength	Uniform elongation	Total elongation
Homogenized	54 μm	282 \pm 7 MPa	725 \pm 11 MPa	0.554 \pm 0.064	0.679 \pm 0.074
Annealed	55 μm	278 \pm 8 MPa	719 \pm 9 MPa	0.535 \pm 0.055	0.697 \pm 0.061

isotopes, etc. [14,15]. APT analyzes elemental distribution inside of the specimen, so that it can avoid the effect of oxidation which might become a problem in prolonged observation by TEM using thin foil specimens. APT may provide reliable elemental information about MEAs/HEAs consisting of elements with similar atomic numbers, which is difficult to obtain using other techniques [16–18]. However, atomic-scale spatial resolution is necessary to investigate SRO in real space because the modulation range of the elemental distribution in SRO is expected to be on the order of a few nearest neighbor distances. Although APT has subnanometer spatial resolution, such a resolution can only be achieved along the needle axis. The spatial resolution along the needle axis (z direction) is higher than that along x and y directions perpendicular to the needle axis of APT specimens. This is because the z position is determined from the sequence of electrical field-evaporated ions, while the x and y positions are obscured due to trajectory aberrations associated with the electrical field-evaporation of ions [19]. As a result, the presence of the atomic planes can be observed only along the needle axis. Accordingly, we fabricated the needle specimens so that the specific crystalline directions coincided with the needle axes in the present study. By using correlative use of TEM and APT [20], atom maps were obtained after checking the crystalline direction along the needle axis by TEM. Existence of SRO was investigated via one-dimensional spatial distribution maps (SDMs) along the specific crystalline direction parallel to the needle axis, as much research work has [21–26]. Additionally, mechanical properties of the specimens heat treated under the same conditions as the APT specimens were evaluated to confirm the effect of SRO on the strength of the CoCrNi MEA. We would like to additionally mention that measures for SRO in solid-solution systems by APT such as atomic clustering algorithms [27] and generalized multicomponent Warren-Cowley SRO parameters [28] have been developed besides those from SDMs along the specific crystalline direction employed in this study.

II. EXPERIMENTAL

An equiatomic CoCrNi alloy was fabricated by vacuum arc-melting and casting. The alloy was cold rolled to 30% reduction in thickness, and homogenized at 1100 °C for 24 h, resulting in a fully recrystallized microstructure. This sample is designated as the homogenized sample hereafter. The mean grain size (d) of the homogenized sample was measured as 54 μm by the line intercept method based on scanning electron microscope (SEM) images of the microstructure. The homogenized sample was annealed at 700 °C for 384 h, where the FCC single-phase was stable [29], designated afterward as the annealed sample. Water quenching was performed after each heat treatment. It should be noted that the above heat treatment

condition was considered to be sufficient for atoms to diffuse long distance for achieving either near-random (1100 °C) or SRO distributions (700 °C) [30]. Grain growth during annealing at 700 °C was negligible, as shown in Table I.

Needle specimens for APT analysis were fabricated by a focused ion beam (FIB) in a SEM dual-beam system (Helios nanoLab600i, FEI). The grains used for the site-specific FIB lift-out were chosen by checking the crystal orientation of the grain using the electron back scattered diffraction (EBSD, OIM, TSL) method. Prior to the FIB milling process, the surfaces of the samples were coated with a Pt layer to prevent damage by Ga-ion bombardment during FIB processing. The needle specimens were sharpened by the annular milling technique, in which the outer and inner diameters of a circular mask were decreased progressively. The needle specimens were fabricated so that the [001] or [111] direction coincided with the needle axis, taking into consideration that the spatial resolution along the needle axis is higher than that along the lateral directions in APT analysis, as was mentioned above.

The crystalline direction along the needle axis was checked using a transmission electron microscope (TEM, JEM-2100plus, JEOL) operated at 200 kV prior to APT measurements. Ar ion milling (Gentle Mill, Technoorg Linda) with an acceleration energy of a few hundred eV was performed on the needle specimens to remove the Ga damage region introduced by FIB processing before TEM observations.

APT analysis was performed using a local electrode atom probe (LEAP4000XHR, Cameca) in a voltage-pulsing mode at a pulse fraction of 20%. The temperature of the needle specimen during the measurement was 35 K. Three-dimensional (3D) atom maps were reconstructed to be consistent with the interplanar spacing of the (001) or (111) planes whose values are 0.1763 and 0.2036 nm, respectively, using dedicated software (IVAS, Cameca).

Tensile tests of the homogenized and annealed samples were conducted three times for each sample at room temperature with a quasistatic strain rate of $8.3 \times 10^{-4} \text{ s}^{-1}$. Small-scale dog-bone-shaped sheet-type tensile specimens with a gauge dimension of 2 mm (length) \times 1 mm (width) \times 1 mm (thickness) were used. Elongation of the specimen during the tensile test was precisely measured by digital image correlation method using Vic-2D software [31]. Our previous studies have showed that the above methods can give us reliable stress-strain data equivalent to those obtained from standard large tensile specimens with strain gauges (e.g., Ref. [32]).

III. RESULTS

Figure 1(a) shows the TEM image and diffraction pattern of the needle specimen of the annealed sample before APT

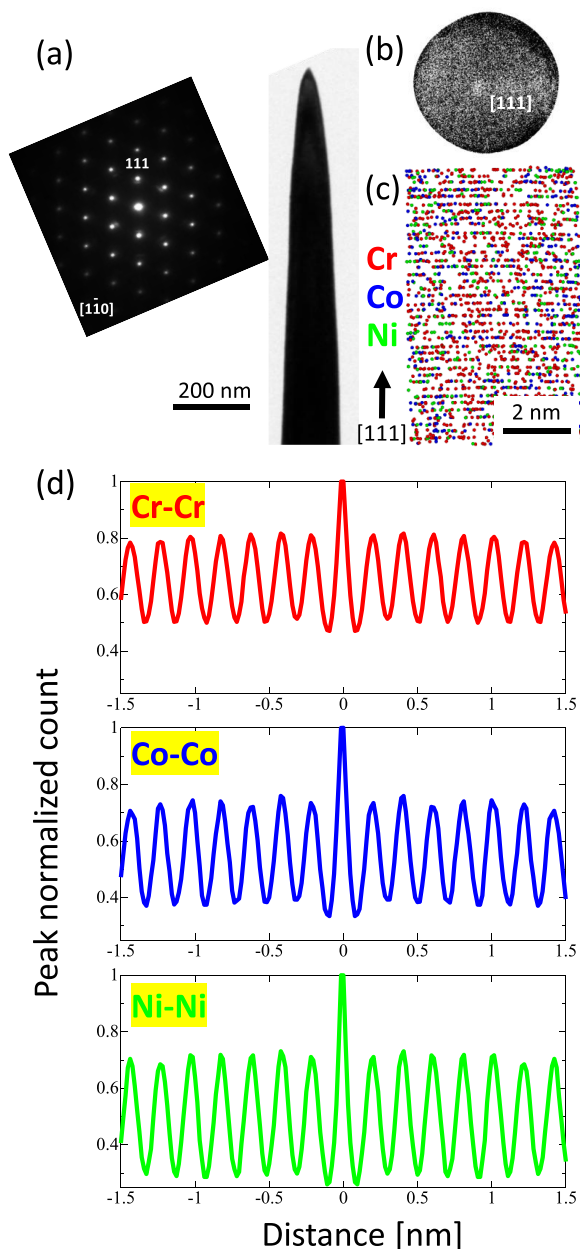


FIG. 1. (a) TEM image and diffraction pattern of the needle specimen fabricated so that the [111] direction coincides with the needle axis in the annealed sample. (b) 2D desorption image showing central pole [111]. (c) Atom map slice (5-nm thick) enlarged in the central pole region. (d) SDM of Cr-Cr, Co-Co, and Ni-Ni along the [111] direction.

measurement. In the TEM observation, the needle specimen was set to the conventional double axes tilting the TEM sample holder (x tilt ± 30 degrees and y tilt ± 20 degrees) so that the needle axis coincided with the axial direction of the TEM sample holder. It should be noted that the x tilt rotates the specimen around the axial direction of the TEM sample holder, while the y tilt rotates the specimen out of the axial direction of the TEM sample holder. The TEM image and diffraction pattern were obtained with y tilt almost equal to zero. The incident direction of the electron beam was ad-

justed using x tilt. It was confirmed that the [111] direction almost coincided with the needle axis in this specimen. Figure 1(b) shows the two-dimensional (2D) desorption image constructed from APT data of Cr, Co, and Ni observed from the needle axis, exhibiting a faint [111] central pole. Figure 1(c) shows an atom map slice (5-nm thick) enlarged in the central pole region of the whole atom map obtained by APT. The vertical direction corresponds to the [111] direction. Each periodic line in the lateral direction in the atom map corresponds to (111) atomic plane of FCC structure. Figure 1(d) shows the SDM of Cr-Cr, Co-Co, and Ni-Ni along the [111] direction. The SDM was obtained from a region of 5 nm \times 5 nm \times 50 nm. The value of the center peak in the SDM was normalized to the unit. The SDM is the autocorrelated calculation of the reconstructed ion positions excluding the contribution from the ion self-correlations, and it can be used to discern specific crystallographic features or structure present in the reconstruction [33]. We employed the SDM in the analysis of SRO to identify possible repeating patterns hidden in the random distributions along the specific crystalline direction. The distance between the peaks in the SDM is the interplanar spacing of (111) plane, which corresponds to 0.2036 nm. The intensities on periodic peaks except for the center peak is almost the same, reflecting that the density of each element on every plane along the [111] direction is almost the same. This indicates that modulation from a random distribution does not occur along the [111] direction.

The same analysis in the [001] direction was carried out using another specimen with [001] parallel to the needle axis. The TEM image and diffraction pattern of the needle specimen of the annealed sample is shown in Fig. 2(a), which confirms that the needle axis is close to the [001] direction. Figure 2(b) represents the 2D desorption image, exhibiting central pole [001] together with zone lines having a fourfold symmetry. The atom map slice (5 nm thick) enlarged in the central pole region along the [001] direction is shown in Fig. 2(c), where the (001) atomic plane is clearly visible. The SDM of each element along the [001] direction is shown in Fig. 2(d). The distance between the peaks in the SDM is the interplanar spacing of the (001) plane corresponding to 0.1763 nm. The peak intensities with a slightly enhanced and depleted value on alternating atomic planes for Cr, Co, and Ni are observed. The intensities are modulated in the range from the central peak to the sixth peak on both sides. Especially, the modulation is relatively strong for Co and Ni, and relatively weak for Cr. This indicates a periodic change in the density of Cr, Co, and Ni on alternating atomic planes along the [001] direction within the range of approximately ten atomic layers, i.e., about 2 nm. Notably, in multicomponent alloys with different field-evaporation strengths of the elements, the atom maps exhibiting aberrations in the atom positions are occasionally obtained due to nonuniform field evaporation. Therefore, we investigated whether the modulation was not due to artifact derived from APT but due to the elemental density variation on the atomic planes along the [001] direction. We investigated the SDM along the [001] direction in the homogenized sample (corresponding to the specimen before annealing) in addition to the annealed sample and compared them to determine the degree of SRO along the [001] direction.

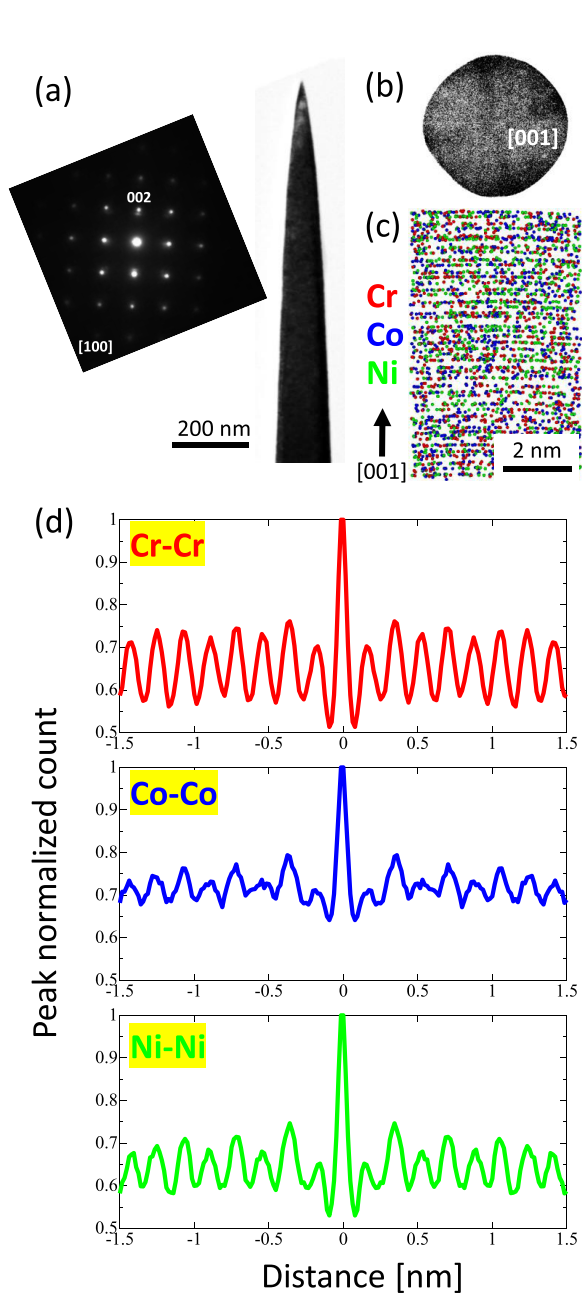


FIG. 2. (a) TEM image and diffraction pattern of the needle specimen fabricated so that the [001] direction coincides with the needle axis in the annealed sample. (b) 2D image shows central pole [001] and zone lines, having a fourfold symmetry. (c) Atom map slice (5-nm thick) enlarged in the central pole region. (d) SDM of Cr-Cr, Co-Co, and Ni-Ni along the [001] direction.

Figures 3(a) shows the TEM image and diffraction pattern of the needle specimen of the homogenized sample fabricated so that the [001] direction coincides with the needle axis. Figure 3(b) is the 2D description image, showing zone lines with central pole [001] clearly exhibiting a fourfold symmetry. Figure 3(c) represents the atom map slice (5-nm thick) along the [001] direction, exhibiting (001) atomic plane. Figure 3(d) is the SDM of each element along the [001] direction. The peak intensities with a slightly enhanced and depleted

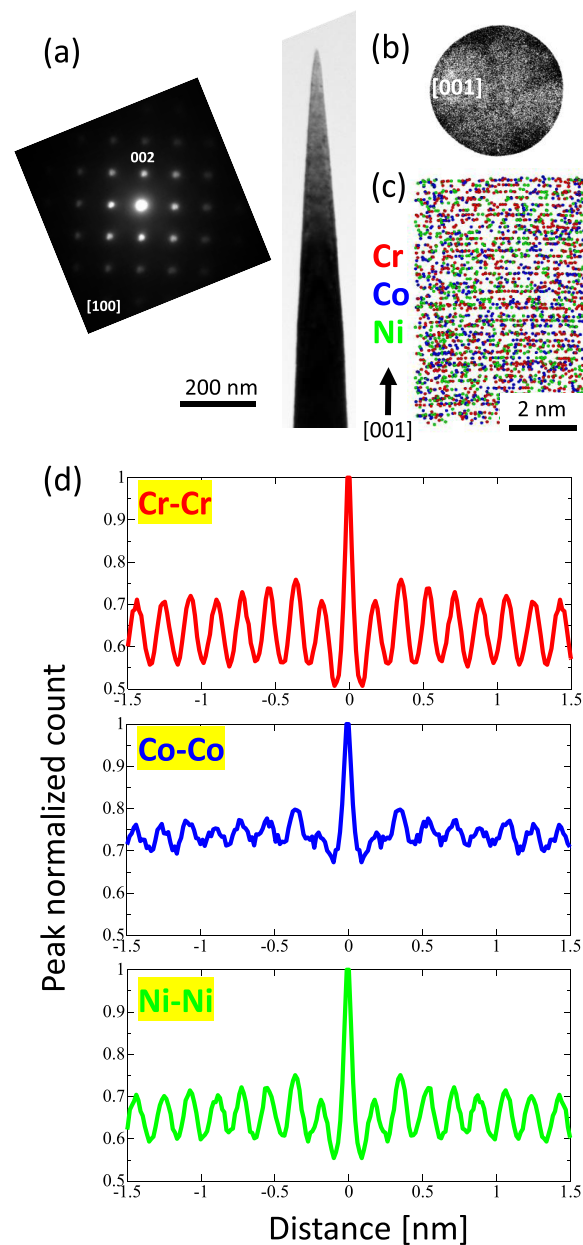


FIG. 3. (a) TEM image and diffraction pattern of the needle specimen fabricated so that the [001] direction coincides with the needle axis in the homogenized sample. (b) 2D image shows central pole [001] and zone lines, having a fourfold symmetry. (c) Atom map slice (5-nm thick) enlarged in the central pole region. (d) SDM of Cr-Cr, Co-Co, and Ni-Ni along the [001] direction.

value on alternating atomic planes for Cr, Co, and Ni are observed. However, the modulated region of the peak intensity is observed only from the center peak to the 2nd peak, which is narrower than the SDM along the [001] direction in the annealed sample. It should be noted that Co has a different signal-to-noise ratio because Co may have high field-evaporation potential around (001) pole compared to Cr and Ni in CoCrNi alloy.

The comparison under the same experimental condition revealed that the degree of the modulation in SDM along the [001] direction changed between the annealed and the

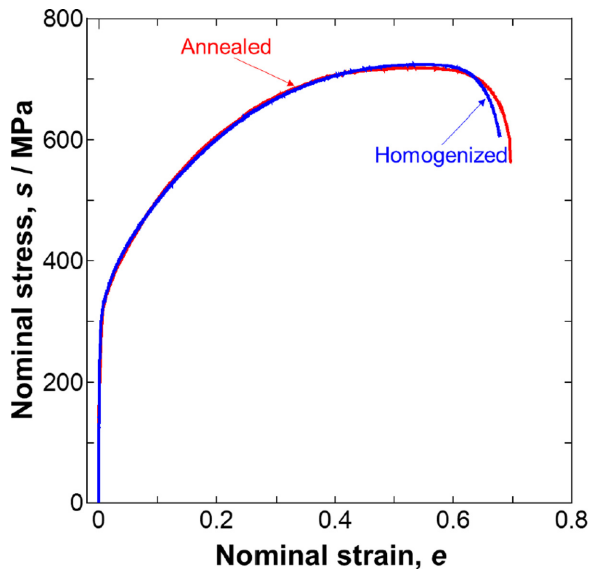


FIG. 4. Nominal stress–nominal strain curves of homogenized (blue) and annealed (red) CoCrNi MEA obtained by tensile tests at room temperature.

homogenized samples. It was confirmed that the degree of modulation range was slightly affected by changing the volume in which the SDM was calculated, but the basic tendency that the modulation range became wider when the heat treatment was performed did not change. This indicated that the modulation did not occur due to artifact derived from APT but due to the elemental density variation on the atomic planes along the [001] direction formed in the annealing heat treatment. The elemental density variation implies the deviation from the random distribution, i.e., the presence of the SRO in the current annealed sample of the CoCrNi alloy. However, it should be noted that the modulated range in the annealed sample is longer than a typical range of SRO. That is, the observed LCO is beyond the short range.

Figure 4 shows engineering–stress–engineering–strain curves of the homogenized and annealed samples having the equivalent grain size obtained by the tensile tests at room temperature. The grain size, yield strength, ultimate tensile strength, uniform elongation, and total elongation are summarized in Table I. It was found that two curves well coincided to each other, indicating the LCO had no impact on the mechanical properties of the CoCrNi alloy.

IV. DISCUSSION

From the SDMs along the [001] and [111] axes, the densities of Cr, Co, and Ni on the atomic planes along [001] were modulated, while those on the atomic planes along the [111] direction were not modulated in the face-centered-cubic CoCrNi solid solution alloy. The same modulation must have occurred along the various $\langle 001 \rangle$ directions, including [100] and [010] on the (001) plane, because of the crystallographic equivalence. Hereafter, we discuss the LCO in the present alloy under the assumption that the modulation occurs along the $\langle 001 \rangle$ direction. The modulated range along $\langle 001 \rangle$ in the annealed sample reached approximately 10 atomic layers, i.e.,

about 2 nm. This means that domains of a few nm range having the LCO existed in the annealed alloy. In general, SRO is expected to be a preferential local ordering of the elements within regions in the order of a few nearest neighbor spacings. We should consider relatively long-range regularity compared with typical SRO, in order to explain the current experimental results. In other words, the LCO domain in this annealed alloy shows somehow an aspect like an intermetallic compound which displays rather long-range ordering (LRO) of atoms on two or more sublattice. However, the intermetallic compound is structurally distinct from solid solution. It should be noted that the diffraction pattern originated from the intermetallic compound was not observed in the TEM observation in the present CoCrNi alloy [Figs. 1(a) and Fig. 2(a)]. Therefore, the LCO domain in this annealed alloy is likely to be a local incomplete LRO domain. Then, assuming that the LCO observed by APT was a precursor of the coherent cluster, we investigated whether the local chemical ordering took the structure similar to the representative coherent cluster such as $L1_2$ and $L1_0$ in the FCC structure. It should also be noted that the quantitative information is difficult to obtain from the SDMs because it depends on the number density of the domain and regularity inside the domain. Therefore, this paper can give only qualitative information.

Considering a unit cell, the $L1_2$ structure consists of the elements at the face centers and those at the cube corners in the unit cell. Accordingly, the center-height (001) plane in the unit cell comprises of only the elements of the face centers, while the bottom and top (001) planes in the unit cell comprise of the elements of the cube corners along with those of the face centers, which is a mixed atomic plane. Densities of both elements on the atomic plane differ between the center height (001) and bottom/top (001) planes. As a result, the elemental densities on the atomic plane along the $\langle 001 \rangle$ direction are modulated. The degree of the modulation of the elements of the cube corners are stronger than those of the face centers. On the other hand, the mixed atomic plane of $\{111\}$ is repeated along the $\langle 111 \rangle$ direction. The elemental densities on the atomic planes along the $\langle 111 \rangle$ direction were equal and not modulated. Consequently, if we assume that the LCO has a structure similar to $L1_2$ in the CoCrNi alloy, the current experimental results that the SDM in APT is not modulated along the [111] direction but modulated along the [001] direction can be explained.

In the case of the $L1_0$ unit cell structure, different kinds of elements alternatively occupy the center-height (001) planes of a tetragonally distorted FCC unit cell. Three kinds of variants $L1_0$ -(100), (010), (001) exist in such a case. According to the 1D SDM analysis along the [001] direction, only the $L1_0$ -(001) variant contributed to the elemental density modulation, whereas the $L1_0$ -(100), (010) variants did not. As for the $\langle 111 \rangle$ direction, the elemental density was not modulated, similar to the case of $L1_2$ structure. If we assume the LCO has a structure similar to $L1_0$ in the CoCrNi alloy, the current experimental results can be also explained.

According to Ref. [34], binary mixing enthalpies for Co–Ni, Cr–Co, and Cr–Ni are 0, +6.8, and +6.4 kJmol⁻¹, respectively, suggesting that Co and Ni are easily mixed in a random manner, while Cr tends to have a repulsive interaction with Co and Ni. If the LCO similar to $L1_2$ is assumed, it

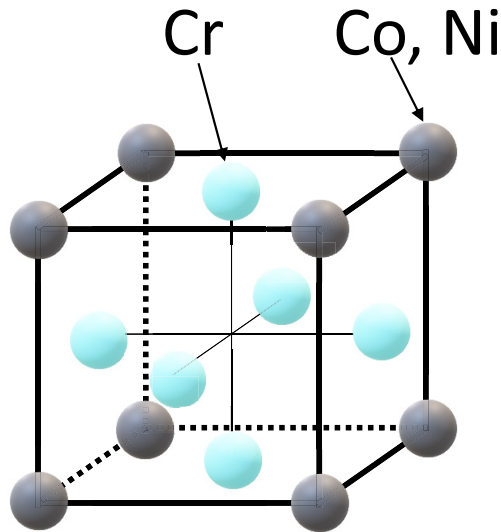


FIG. 5. Schematic illustration of the expected structural model of the LCO in CoCrNi MEA. It should be noted that this figure does not reflect the quantitative information.

is expected that Cr atoms tend to occupy the face-centered positions to aggregate, while Co and Ni tend to occupy the cube-corner positions (similar to the $L1_2$ structure in Cr-Ni system [35]) as shown in Fig. 5, which is consistent with the present SDM results (Fig. 2). If the LCO similar to $L1_0$ is assumed, aggregation of Cr in one of the $\{001\}$ plane with accompanying slight lattice distortion in the normal direction is expected. If Cr tends to aggregate in the plane, it is expected that the modulation of Cr is stronger than that of Co and Ni. The degree of the elemental density modulation is not consistent with the SDM results. It can be concluded, therefore, that $L1_2$ -type LCO seems more probable to form in the current annealed samples than the $L1_0$ -type.

In this study, the presence of LCO in the annealed CoCrNi alloy was confirmed by APT. However, there was no difference in the mechanical properties between the homogenized sample and the annealed sample, as shown in Table I, which indicated that the LCO observed in this study did not affect the mechanical properties of the CoCrNi alloy. Zhang *et al.* [10] reported that the yield stress (255 MPa) of the sample, in which SRO was confirmed by TEM, was higher than that of the homogenized sample obtained by water quenching after heat treating at 1200 °C for 48 h (205 MPa), which seems inconsistent with our results. One possibility is that the degree of LCO development depends on the heat treatment condition. Namely, the degree of LCO in the sample of Zhang heat-treated at 1000 °C and then furnace cooled [10] was

more developed than that in the present study annealed at 700 °C and water quenched. It should be noted that the yield strength of the homogenized and the annealed samples in the current study (~ 280 MPa) was higher than that of the sample heat-treated at 1000 °C followed by water quenching (205 MPa) reported by Zhang *et al.* [10]. This can be reasonably explained by the difference in the grain size. The grain size of the current samples was 54 or 55 μm as shown in Table I, while that of Zhang *et al.* was about 800 μm , equivalent to about 60 MPa difference in yield strength, according to the Hall-Petch relationship of the CoCrNi alloy obtained in our previous studies [9,32]. In the conventional research on the CoCrNi alloys, except for that by Zhang *et al.* [10], the annealing of the alloy was followed by fast cooling like the present study. Finally, it can be concluded that LCO is formed in the CoCrNi alloy, but the degree of LCO formed by the annealing in this study does not affect the strength of the alloy. The latter is consistent with the conclusion by Yin *et al.* [9] that the effect of SRO on the strength is negligible in the MEA processed under ordinary annealing conditions.

V. CONCLUSION

The local structure of the equiatomic CoCrNi alloy was investigated by APT. The spatial distribution map analysis demonstrated that the elemental density along the $[001]$ direction was modulated, while that along the $[111]$ direction was not modulated. It was shown that the modulated region reached to 10 atomic distances (~ 2 nm), which was much larger than the size of typical short-range ordering. The results suggested that Cr-rich $\{001\}$ atomic layers and (Ni + Co)-rich $\{001\}$ layers tended to align mutually in the CoCrNi alloy with FCC structure. This modulation could be attributed to the presence of the local chemical ordering that took the structure similar to $L1_2$ or $L1_0$. The degree of the modulation suggested that the structure similar to $L1_2$ was more likely to form. The mechanical properties of the material did not change despite the presence of local chemical ordering, implying that the local chemical ordering in the CoCrNi alloy heat treated under the present condition had no impact on the strength of the alloy.

ACKNOWLEDGMENTS

The authors acknowledge financial support from the MEXT-KAKENHI Grant-in-Aid for Scientific Research on Innovative Areas “High Entropy Alloys” (No. JP18H05455 and JP18H05456) and the Grant-in-Aid for JSPS (Japan Society for Promotion of Science) Research Fellow (No. JP18J20766), all through the Ministry of Education, Culture, Sports, Science, and Technology (MEXT), Japan.

- [1] D. B. Miracle and O. N. Senkov, *Acta Mater.* **122**, 448 (2017).
- [2] B. S. Murty, J. W. Yeh, S. Ranganathan, and P. P. Bhattacharjee, *High-Entropy Alloys*, 2nd. ed. (Elsevier, Amsterdam, 2019), p.195.
- [3] O. N. Senkov, D. B. Miracle, and K. J. Chaput, *J. Mater. Res.* **33**, 3092 (2018).

- [4] E. P. George, W. A. Curtin, and C. C. Tasan, *Acta Mater.* **188**, 435 (2020).
- [5] B. Cantor, I. T. H. Chang, P. Knight, and A. J. B. Vincent, *Mater. Sci. Eng. A* **375–377**, 213 (2004).
- [6] Z. Wu, H. Bei, G. M. Pharr, and E. P. George, *Acta Mater.* **81**, 428 (2014).

- [7] Z. Li, S. Zhao, R. O. Ritchie, and M. A. Meyers, *Prog. Mater. Sci.* **102**, 296 (2019).
- [8] Q. J. Li, H. Sheng, and E. Ma, *Nat. Commun.* **10**, 3563 (2019).
- [9] B. Yin, S. Yoshida, N. Tsuji, and W. A. Curtin, *Nat. Commun.* **11**, 2507 (2020).
- [10] R. Zhang, S. Zhao, J. Ding, Y. Chong, T. Jia, C. Ophus, M. Asta, R. O. Ritchie, and A. M. Minor, *Nature (London)* **581**, 283 (2020).
- [11] J. M. Cowley, *Phys. Rev.* **77**, 669 (1950).
- [12] J. M. Cowley, *Phys. Rev.* **120**, 1648 (1960).
- [13] F. X. Zhang, S. Zhao, K. Jin, H. Xue, G. Velisa, H. Bei, R. Huang, J. Y. P. Ko, D. C. Pagan, J. C. Neufeind, W. J. Weber, and Y. Zhang, *Phys. Rev. Lett.* **118**, 205501 (2017).
- [14] T. F. Kelly, in *Springer Handbook of Microscopy* edited by P. W. Hawkes, and J. C. H. Spence (Springer, Chad, Switzerland, 2019), p. 715.
- [15] B. Gault, M. P. Moody, J. M. Cairney, and S. P. Ringer, *Mater. Today* **15**, 378 (2012).
- [16] K. G. Pradeep, N. Wanderka, P. Choi, J. Banhart, B. S. Murty, and D. Raabe, *Acta Mater.* **61**, 4696 (2013).
- [17] B. Han, J. Wei, Y. Tong, D. Chen, Y. Zhao, J. Wang, F. He, T. Yang, C. Zhao, Y. Shimizu, K. Inoue, Y. Nagai, A. Hu, C. T. Liu, and J. J. Kai, *Scr. Mater.* **148**, 42 (2018).
- [18] Y. Tong, D. Chen, B. Han, J. Wang, R. Feng, T. Yang, C. Zhao, Y. L. Zhao, W. Guo, Y. Shimizu, C. T. Liu, P. K. Liaw, K. Inoue, Y. Nagai, A. Hu, and J. J. Kai, *Acta Mater.* **165**, 228 (2019).
- [19] B. Gault, B. Klaes, F. F. Morgado, C. Freysoldt, Y. Li, F. De Geuser, L. T. Stephenson, and F. Vurpillot, [arXiv:2103.01665](https://arxiv.org/abs/2103.01665) (2021).
- [20] M. Herbig, *Scr. Mater.* **148**, 98 (2018).
- [21] E. A. Marquis, *Microsc. Microanal.* **13**, 484 (2007).
- [22] B. P. Geiser, T. F. Kelly, D. J. Larson, J. Schneir, and J. P. Roberts, *Microsc. Microanal.* **13**, 437 (2007).
- [23] B. Gault, X. Y. Cui, M. P. Moody, F. De Geuser, C. Sigli, S. P. Ringer, and A. Deschamps, *Scr. Mater.* **66**, 903 (2012).
- [24] R. K. W. Marceau, A. V. Ceguerra, A. J. Breen, M. Palm, F. Stein, S. P. Ringer, and D. Raabe, *Intermetallics* **64**, 23 (2015).
- [25] S. Meher, T. Rojhirunsakool, P. Nandwana, J. Tiley, and R. Banerjee, *Ultramicroscopy* **159**, 272 (2015).
- [26] S. Meher, P. Nandwana, T. Rojhirunsakool, J. Tiley, and R. Banerjee, *Ultramicroscopy* **148**, 67 (2015).
- [27] R. K. W. Marceau, G. Sha, R. Ferragut, A. Dupasquier, and S. P. Ringer, *Acta Mater.* **58**, 4923 (2010).
- [28] A. V. Ceguerra, M. P. Moody, R. C. Powles, T. C. Petersen, R. K. W. Marceau, and S. P. Ringer, *Acta Crystallogr.* **A68**, 547 (2012).
- [29] B. Schuh, B. Volker, J. Todt, K. S. Kormout, N. Schell, and A. Hohenwater, *Materials (Basel)* **11**, 662 (2018).
- [30] K. Jin, C. Zhang, F. Zhang, and H. Bei, *Mater. Res. Lett.* **6**, 293 (2018).
- [31] H. Schreier, J. J. Orteu, and M. A. Sutton, Image correlation for shape, motion and deformation measurements: Basic concepts, in *Theory and Applications* (Springer US, Boston (2009).
- [32] S. Yoshida, T. Bhattacharjee, Y. Bai, and N. Tsuji, *Scr. Mater.* **134**, 33 (2017).
- [33] D. J. Larson, T. J. Prosa, R. M. Ulfig, B. P. Geiser, and T. F. Kelly, *Local Electrode Atom Probe Tomography: A User's Guide* (Springer, New York, 2013), p. 185.
- [34] K. Y. Tsai, M. H. Tsai, and J. W. Yeh, *Acta Mater.* **61**, 4887 (2013).
- [35] N. Clement, D. Caillard, and J. L. Martin, *Acta Metall.* **32**, 961 (1984).